JOURNAL OF SPACECRAFT AND ROCKETS
Vol. 39, No. 4, July–August 2002

Drag Reduction on Blunt-Based Vehicles Using Forebody Surface Roughness

Stephen A. Whitmore*
Naval Postgraduate School, Monterey, California 93943
and
Jonathan W. Naughton†
University of Wyoming, Laramie, Wyoming 82071

Results of wind-tunnel tests that demonstrate a novel drag reduction technique for blunt-based vehicles are presented. For these tests, the forebody roughness of a blunt-based model was modified using micromachined surface overlays. As forebody roughness increases, the boundary layer at the model aft thickens and reduces the shearing effect of external flow on the separated flow behind the base region, resulting in reduced base drag. For vehicle configurations with large base drag, existing data predict that a small increment in forebody friction drag will result in a relatively large decrease in base drag. If the added increment in forebody skin drag is optimized with respect to base drag, reducing the total drag of the configuration is possible. The wind-tunnel tests results conclusively demonstrate the existence of a forebody drag–base drag optimal point. The data demonstrate that the base drag coefficient corresponding to the drag minimum lies between 0.225 and 0.275, referenced to the base area. Most important, the data show a drag reduction of approximately 15% when the drag optimum is reached.

Nomenclature

a_0, a_1, a_2, a_3	=	forebody pressure distribution curve-fit coefficients
b_0, b_1, b_2, b_3, b_4	=	base pressure distribution curve-fit coefficients
$C_{D_{\text{base}}}$	=	base pressure drag coefficient
$C_{D_{\text{forebody}}}$	=	forebody pressure drag coefficient
C_{D_0}	=	zero-lift freestream total drag coefficient
C_F	=	viscous forebody drag coefficient
C_p	=	pressure coefficient
c_{fx}	=	local skin-friction coefficient
D'	=	section drag, Nt/m
$\mathrm{d}P_e/\mathrm{d}x$	=	longitudinal pressure gradient on model, kPa/m
$\mathrm{d}\theta/\mathrm{d}x$	=	longitudinal gradient of the boundary-layer momentum thickness
H	=	wake or boundary-layer shape parameter, δ/θ
h_{base}	=	base height, cm
L	=	model length, cm
$u_{\min}$	=	minimum velocity in wake velocity profile, m/s
$u(y)$	=	local velocity distribution in wake or boundary layer, m/s
V_e	=	velocity at the edge of the wake or boundary layer, m/s
y	=	lateral coordinate for wake or boundary layer or base area, cm
β	=	Clauser[11] pressure gradient parameter
δ	=	wake half-width, local boundary-layer thickness, cm
δ^*	=	boundary-layer displacement thickness, cm
δ_w^*	=	wake displacement thickness, cm
Θ	=	forebody incidence angle, deg
θ	=	forebody surface incidence angle, deg
θ_w	=	wake momentum thickness, cm
θ_∞	=	freestream momentum thickness, cm
κ	=	law-of-the-wake slope parameter
κ_s	=	equivalent sand grain roughness, cm
Λ	=	land width, cm
Π	=	wake parameter
ρ	=	air density, kg/m^3
Σ	=	slot width, cm
σ	=	standard deviation
τ	=	shim thickness, cm

Introduction

MANY of the designs advocated for the current generation of transatmospheric reusable launch or space-access vehicles are derived from variations of the original lifting-body concept. For a variety of reasons,[1] these designs all have large, rather blunt base areas compared with those of conventional aircraft. These blunt base areas are generally highly separated and result in large negative base pressure coefficients. Because of the large base-to-wetted-area ratios of these space vehicles, the base drag comprises the majority of the overall vehicle drag. The resulting low lift-to-drag ratios result in very steep approach glide slopes. These steep approach angles present difficult energy management tasks for autonomous reentry systems. Any decrease in base drag potentially can significantly improve the overall vehicle performance and make the autonomous reentry and landing task less difficult.

A body of early experimental work conducted in the late 1950s and early 1960s by Hoerner[2] offers a potential solution to the reusable launch vehicle base drag problem. For blunt-based objects with heavily separated base areas, a correlation between the base pressure drag and the viscous component of the forebody drag has been demonstrated. This paper presents the results of a series of wind-tunnel experiments that exploit this forebody-to-base drag relationship to reduce the overall drag of a simple blunt-based configuration by adding precise levels of roughness to the forebody.

Received 9 February 2001; revision received 2 July 2001; accepted for publication 26 February 2002.

*NASA Chair Professor, Space Systems Academic Group, 589 Dyer Road, 201c Root Hall. Associate Fellow AIAA.

†Assistant Professor, Department of Mechanical Engineering, P.O. Box 3295. Senior Member AIAA.

Background

For blunt-based objects whose base areas are heavily separated, a clear relationship between base drag and the viscous forebody drag has been demonstrated by Hoerner.[2] In this paper, the viscous forebody drag is defined as the axial projection of the integral of all viscous forces acting on the vehicle forebody. These viscous forces include surface skin friction, frictional effects of forebody flow separation, and parasite drag. Axial forces resulting from the forebody pressure distribution are considered separately from the viscous forebody drag. Figure 1 shows subsonic drag data and curve fits taken from Hoerner[2] for two-dimensional and three-dimensional projectiles. An important feature of the data presented here is the trend for decreasing base drag as the viscous forebody drag increases. This base drag reduction is highly correlated to the state of the boundary-layer effects at the aft base end of the vehicle.

Hoerner[2] speculates that the surface boundary layer acts as an insulator between the external flow and the separated air behind the base. As the forebody drag increases, the boundary-layer thickness at the forebody aft also increases. This increase reduces the effectiveness of the jet pump caused by the shearing of the external flow on the separated flow behind the base region. Other studies[3,4] have shown that the increased boundary-layer thickness may also serve to reduce the strength of the von Kármán vortex street that trails behind the separated base area (see Ref. 2). As such, the boundary increased boundary layer at the aft end acts in much the same way as a splitter plate. When the uniformity of the evenly spaced within the wake is disrupted, the base drag is reduced.

Vehicle configurations with large base drag coefficients lie on the steep portion of Hoerner's[2] curve, where a small increment in the forebody friction drag will result in a relatively large decrease in the base drag. Conceptually, if the added increment in viscous forebody drag is optimized with respect to the base drag, then a reduction in the overall drag of the configuration may be possible. Figure 2 illustrates this drag optimization, based on the curve fits of Hoerner's data. These data clearly illustrate the concept of a drag bucket.

Another important feature of the data shown in Figs. 1 and 2 is that for the same viscous forebody drag, two-dimensional objects tend to have a significantly larger base drag than three-dimensional objects. In general, the base flow around three-dimensional objects is characterized by very-broadband (frequency) flow disturbances; the periodic flow phenomenon is far less pronounced than for two-dimensional objects. The base pressure under nonperiodic (three-dimensional) flow conditions is considerably higher (equating to lower base drag) than under similar conditions in a periodic (two-dimensional) flow.

The ramifications of this two-dimensional/three-dimensional base drag difference become extremely important when one considers full-scale, high-Reynolds-number flight vehicles. Saltzman et al.[5] have compiled subsonic drag data from vehicles configured for hypersonic flight. This compendium includes flight data for the X-15, M2-F1, M2-F3, X-24A, and X-24B vehicles; the space shuttle; and the Linear Aerospike SR 71 Experiment (LASRE). These data are compared to the two- and three-dimensional mathematical models derived from Hoerner's[2] data in Fig. 3. The full-scale flight data agree more closely with the two-dimensional curve than the three-dimensional curve. For full-scale configurations, the flow appears to be locally two dimensional and allows the trailing vortex street to become well established. Figure 4 shows direct visual proof of this assertion because a periodic vortex structure is clearly visible trailing behind the M2-F1 vehicle. The data shown in Figs. 1–3 imply that the base separation on large-scale, blunt-based vehicles

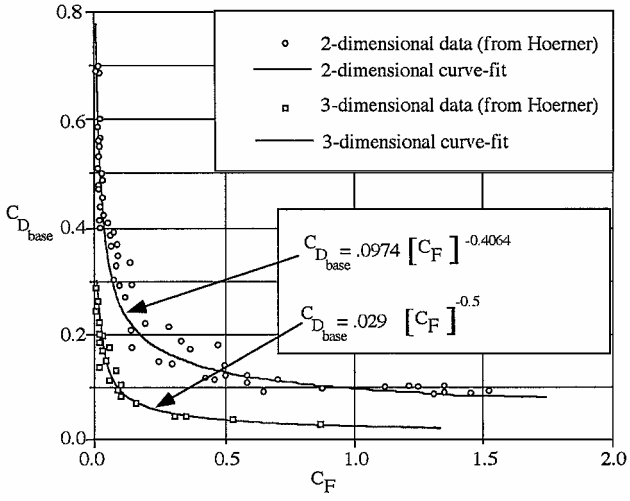

Fig. 1 Effect of viscous forebody drag on base drag of a blunt-based projectile.

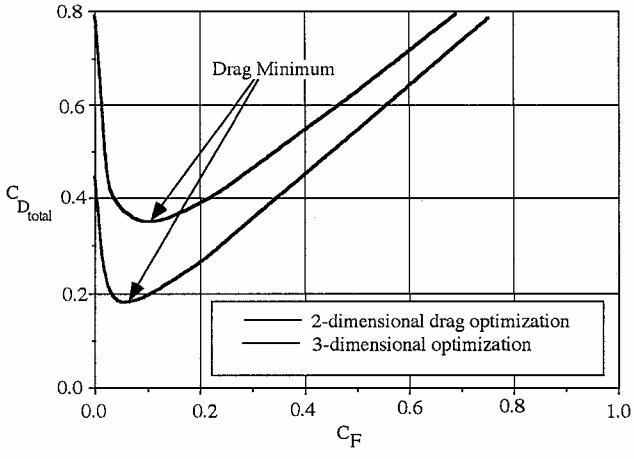

Fig. 2 Predicted drag bucket.

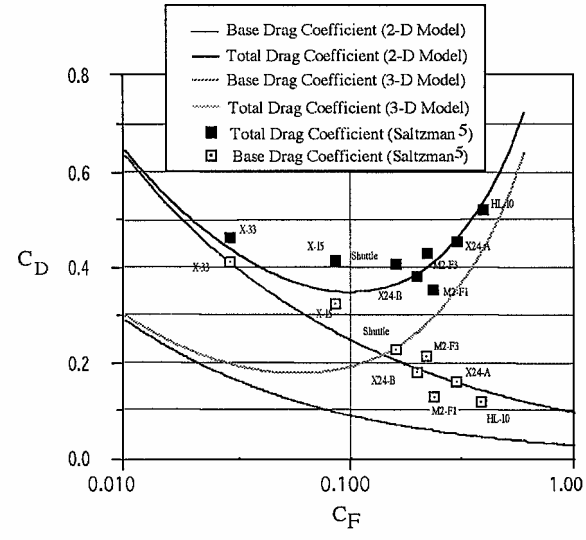

Fig. 3 Comparison of flight data to Hoerner[2] drag models.

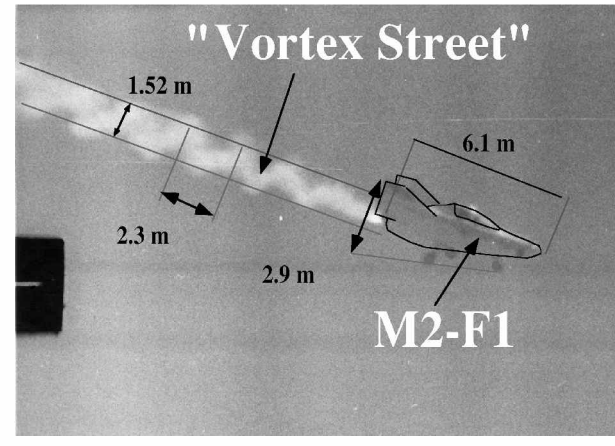

Fig. 4 Von Kármán vortex street formation trailing the M2-F1 vehicle.

behaves in a quasi-two-dimensional manner. Consequently, configurations with a base drag coefficient greater than approximately 0.30 (referenced to the base area) will lie on the left side of Hoerner's[2] curve. These configurations may be considered to be suboptimal with respect to the viscous forebody drag coefficient. Incrementally increasing the viscous forebody drag theoretically should lower the overall drag of the configuration.

Flight Tests

Flight-test results from the LASRE drag reduction experiment[6] provide some incomplete validation of the preceding hypothesis. The LASRE was a flight test of an approximately 20% half-span model of an X-33 forebody model mounted on top of the NASA SR-71 aircraft. A piggyback experiment on the LASRE program sought to reduce base drag by adding a small amount of surface roughness to the model forebody. The model was instrumented with load cells that allowed a six-degree-of-freedom measurement of forces and moments and with surface pressure ports that allowed the model forebody pressure and base drag to be numerically integrated.

The LASRE verified that the base drag was reduced by as much as 15%; unfortunately, the overall drag of the configuration was not reduced. The methods for applying the forebody sand-grain roughness were believed to be too crude to achieve an overall drag reduction. Clearly, to prove the existence of a drag optimum, further tests under a more precisely controlled flow environment were required.

Wind-Tunnel Tests

A series of low-speed, two-dimensional wind-tunnel tests was conducted to study the potential for minimizing the total configuration drag using surface roughness increments. In these tests, a leading-edge cylinder with a blunt afterbody was tested. The full-scale flight data (Figs. 3 and 4) demonstrate that the results of the two-dimensional tests should be generally applicable to large-scale, three-dimensional vehicles. In fact, with regard to the comparisons shown in Fig. 3, tests performed using two-dimensional models were believed to be more representative of the large-scale flight vehicles than those performed with three-dimensional models. The series of tests had two primary objectives:

1) Test the hypothesis regarding forebody roughness in a systematic manner to conclusively demonstrate existence of a viscous forebody drag–base drag optimum (the drag bucket).

2) Establish a criterion for when forebody drag is suboptimal, that is, at what point increasing forebody drag results in an overall drag reduction.

Wind-Tunnel Model Description

Figure 5 shows a three-view drawing of the wind-tunnel model. The machined-aluminum model consists of a 2.54-cm (1-in.)-diam cylindrical leading edge with a flat-sided afterbody 11.43 cm (4.5 in.) long. Removable aluminum plates on the sides of the model allow various levels of surface roughness to be tested by interchanging the plates. The base-to-wetted area of the model is approximately 10.7%.

Bonding micromachined brass overlays to the side plates modified forebody roughness. These screens consist of a series of transverse bars with the shim τ, slot Σ, and "land" Λ dimensions determining the roughness of the surface. Figure 6 shows the geometric layout for these bar grid overlays. For all but one configuration, the slots and lands were transverse to the direction of the freestream flow. A single overlay geometry using lands and slots aligned

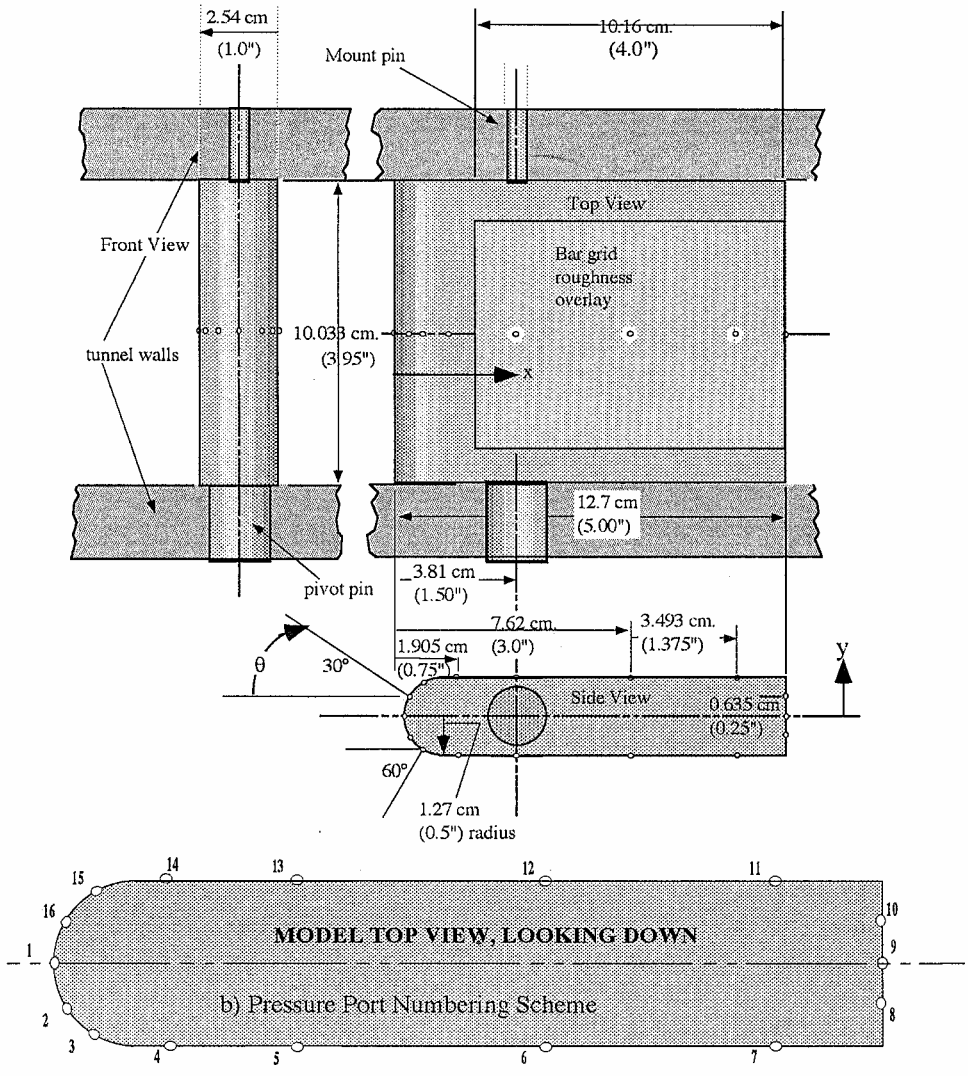

Fig. 5 Three views of wind-tunnel model.

parallel to the direction of flow was also tested. Table 1 shows the geometries tested and the equivalent sand-grain surface roughness κ_s calculated using empirical formulas presented by Mills.[7]

Wind-Tunnel Description

The model was tested in a low-speed wind tunnel at NASA Dryden Flight Research Center (Edwards, California). The ambient, open-cycle tunnel has a test section approximately 10 by 25 cm. An ac motor uses a squirrel-cage fan located at the downstream end to pull air through the tunnel. When the model was mounted in the tunnel test section, the total blockage was 10%. This level of blockage is considered high for traditional wind-tunnel testing. The primary effect of the blockage was to accelerate the flow around the model forebody, causing a rise in the dynamic pressure and a drop in the static pressure along the sides of the tunnel wall (outside of the tunnel wall boundary layer). The dynamic pressure rise (static pressure drop) was taken into account by calibrating local dynamic and static pressure ratios, referenced to the dynamic and static pressure ahead of the model, as a function of the axial position in the tunnel. Figure 7 shows this calibration plot. At each longitudinal measurement location, the derived dynamic and static pressure values were used to compute the local pressure coefficient:

$$C_p(x) = \frac{\left[p(x) - p(x)_{(\text{ratio})}\, p_\infty\right]}{q(x)_{(\text{ratio})}\, q_\infty} \tag{1}$$

In Eq. (1), x is the longitudinal coordinate measured aft from the leading edge of the model, $C_p(x)$ is the local pressure coefficient at position x along the model, $p(x)$ is the local static pressure measurement on the surface, and p_∞ and q_∞ are the static and dynamic pressures as measured several model lengths upstream, near the inlet to the wind tunnel. The correction scale factors $p(x)_{\text{ratio}}$ and $q(x)_{\text{ratio}}$ are shown plotted in Fig. 7.

Table 1 Screen overlay roughness dimensions

Configuration number	λ, cm	Σ, cm	τ, cm	κ_s, cm
1	0.0000	0.0000	0.0000	0.0000[a]
2	0.0051	0.0051	0.0051	0.0163[b]
3	0.0254	0.0381	0.0254	0.1143
4	0.0508	0.1016	0.0508	0.2896
5	0.0508	0.2032	0.0508	0.4854
6	0.1016	0.2540	0.1016	0.6911

[a]Smooth model. [b]Parallel bars.

With the model mounted in the wind tunnel, a maximum freestream airspeed of approximately 28.0 m/s was achieved. Based on the model length, this freestream velocity translates to a Reynolds number Re_L of approximately 2.25×10^5. Tests were also performed at airspeeds of approximately 14.6 m/s. The corresponding Reynolds number for these lower-speed tests was approximately 1.25×10^5. The wind-tunnel turbulence intensity levels were sufficiently large that the model flow was turbulent beginning at the leading edge.

Instrumentation

The tunnel was instrumented with series of static pressure taps along the sidewalls of the tunnel. Total (reference) pressure levels were sensed with a pitot probe placed five model lengths ahead of the model. In all, 16 pressure taps were distributed around the centerline of the model: 5 ports on the model forebody, 8 ports placed along the sides of the model, and 3 ports placed on the base. These port locations allowed body pressure forces to be accurately integrated. Figure 5 also shows the locations of the 16 model pressure ports.

The total model drag coefficient was measured by wake velocity profiles sensed using a traversing pitot-static probe. This probe sensed both local total and static pressure values. The probe tip was placed 12.7 cm aft of the model base area. The wake probe tip diameter was approximately 0.025 cm. Similar momentum-defect measurements for skin friction were performed at the model aft end using a traversing boundary-layer pitot probe. For the boundary-layer profiles, the traversing probe measured only local total pressure. Local static pressure was assumed constant across the depth of the model boundary layer. A side port on the tunnel wall sensed freestream static pressure at the model base. The boundary-layer probe tip diameter was approximately 0.02 cm. The probe positions relative to the centerline of the model were measured using a digital micrometer. The estimated accuracy of the digital positioning sensor was approximately 0.0025 cm. Figure 8 shows the wake and boundary-layer probes mounted next to the model in the tunnel.

All of the model, tunnel wall, and traversing probe pressure data were sensed with a highly accurate set of digital (RS-422) scanning

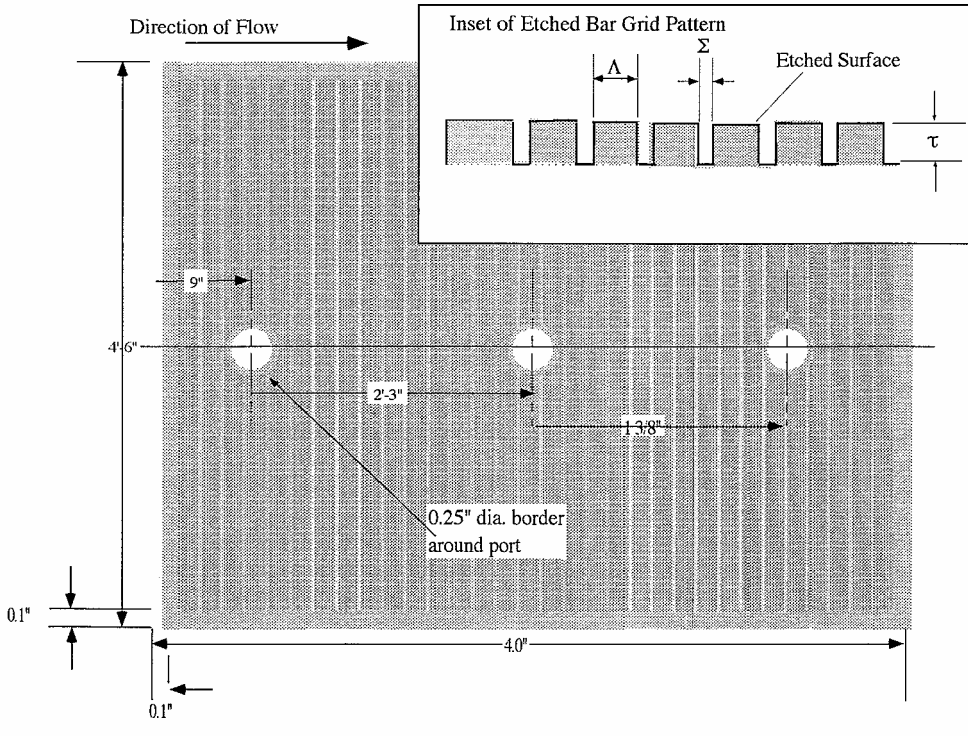

Fig. 6 Schematic of a typical roughness grid overlay.

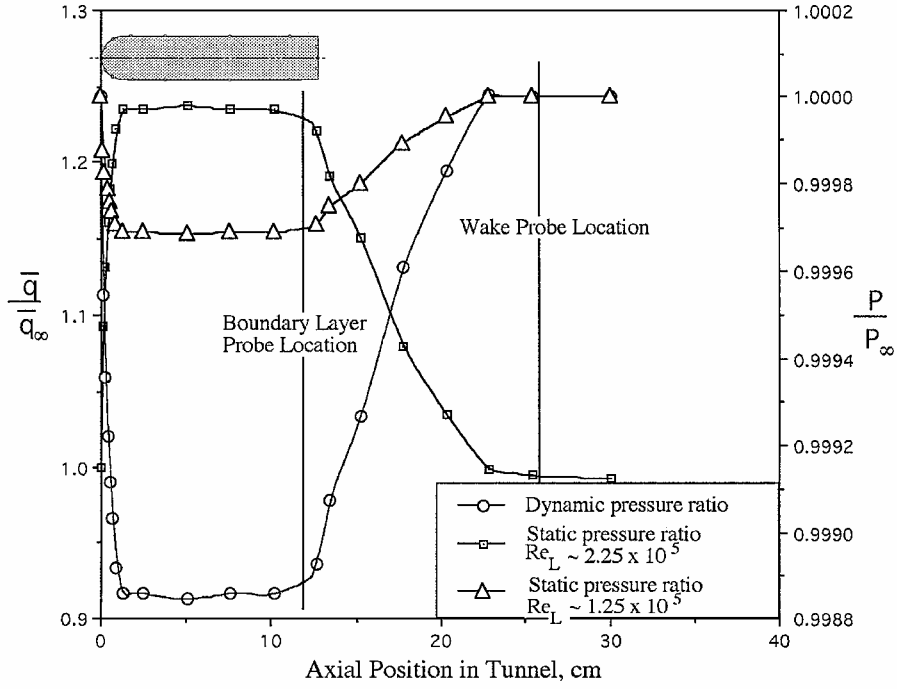

Fig. 7 Dynamic and static pressure calibration for tunnel blockage.

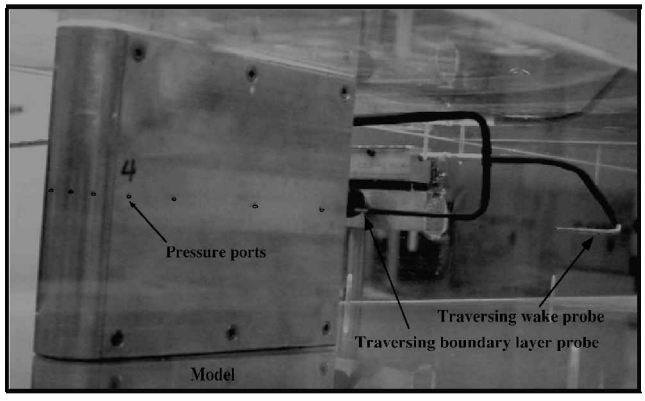

Fig. 8 Model mounted in wind tunnel.

pressure modules. A laptop computer using the serial port to perform individual channel addressing recorded these data. Full-scale span of these differential pressure modules was ±2.490 kPa. The manufacturer's accuracy specifications for the differential pressure measurements are ±0.05% of full scale, or approximately ±0.00125 kPa. The differential pressure transducers were referenced to the pitot probe placed approximately 64 cm ahead of the model. The reference pitot pressure was sensed with a highly accurate absolute pressure manometer. The estimated accuracy for the absolute reference pressure measurement is approximately ±0.010 kPa. The reference temperature was sensed externally to the tunnel using a type T thermocouple with an estimated accuracy of approximately ±0.5°C.

Test Procedures

The low dynamic pressure levels, less than 0.4788 kPa, during this series of wind-tunnel tests required that data be taken with great consistency to minimize the effects of experimental procedure on the overall measurement errors. For all test conditions and configurations, the transducers were zeroed before testing, and the model angle of attack was set to zero by comparison of the left and right surface model pressures. To set the zero angle-of-attack position, the model position was perturbed until the left and right surface pressure curves lay directly on top of each other.

Although the electronically scanned pressure transducers have a built-in feature that allows the transducers to be zeroed online, experimentation determined that a superior level of bias correction was achieved when the transducers were manually zeroed before each data run. Transducer biases were evaluated by taking readings with the tunnel in the off position (zero airspeed). In this zeroing process, each pressure port was addressed a total of 100 times, and these data samples were averaged to minimize the effects of random sensor errors. The resulting zero readings were written to an archival file for later use by postprocessing analysis algorithms.

The pressure scans read data from the 16 model pressure ports as well as the total and static pressure levels in the tunnel. For each configuration tested, that is, each different grid pattern or airspeed, the pressure scans were repeated 10 times. For each of the 10 measurement sequences, the zeroing procedure was performed, and the tunnel was activated and allowed to stabilize. Typically, 100 individual data samples were averaged for each data run to minimize the effects of random measurement errors and tunnel turbulence. After 10 pressure scans were taken for each configuration, the data were converted to pressure coefficients by postprocessing algorithms, and the pressure coefficients data were averaged. The standard deviation of the 10 measurement sequences data was used as a representation of the end-to-end accuracy of the measurement system. Typically the end-to-end pressure coefficient error varied between ±0.003 and ±0.005.

For the wake surveys, each data point consists of a pitot and a static-pressure measurement taken at a single lateral offset from the model centerline. For the boundary-layer surveys, each data point consists of a pitot measurement taken at a lateral offset and a wall static pressure measurement. For each data point, 100 data samples were averaged to minimize the effects of random measurement errors and tunnel turbulence. To define the wake profile completely, approximately 200 y-position data points were required. For early tests in the tunnel, the entire wake profile was measured. These data were so symmetrically distributed that as a time saving and labor measure, later tests only surveyed one-half of the wake profile.

Because of the large number of data samples (approximately 20,000) required to define the wake for each measurement configuration, completing each of the wake surveys 10 times as was done with the pressure survey data was considered impractical. Instead, each wake survey was performed twice and the resulting data were interleaved to form a single local velocity distribution profile. At the beginning of each of the two wake surveys, the probe sensor zero readings were taken and written to an archival file for use by the postprocessing routines. When computed, transducer biases were assumed constant for the duration of each wake survey.

Analysis Methods

This section presents the analysis methods used to interpret the data collected during the wind-tunnel tests. A brief discussion of the error analysis methods is presented at the end of this section.

Wake Velocity Profile Analysis

This analysis method curve fits the wind-tunnel wake data with a symmetric cosine law velocity distribution profile of the form

$$u(y)/V_e = \tfrac{1}{2}[u_{\min}/V_e[1+\cos(\pi y/\delta)] + 1 - \cos(\pi y/\delta)] \quad (2)$$

In Eq. (2), $u_{\min}$ is the minimum velocity in the wake, y is the lateral distance outward from the center of the wake, U_e is the velocity at the edge of the wake, $u(y)$ is the local velocity within the wake, and δ is the wake half-width. A nonlinear least-squares method was used to curve fit the measured velocity distribution data to the profile assumed in Eq. (2). Output variables from the curve-fit routines were $u_{\min}/V_e$ and δ. A detailed development of the nonlinear curve-fitting method used in the wake analysis is presented by Whitmore and Moes.[6]

Figure 9 shows an example wake curve fit compared with the wind-tunnel data. These data were obtained from the smooth model configuration tested at $Re_L = 2.25 \times 10^5$. The turbulent wake extends beyond the lateral boundaries of the wind-tunnel model by approximately 3 cm. The wake structure is symmetric, and the cosine velocity distribution law gives a reasonable curve fit. Note that the center of the wake appears to contain a sizeable amount of turbulence that significantly decreases near the edge of the wake. The velocity profile curve fit, Eq. (2), is substituted into the equations for the wake displacement thickness δ_w, and θ_w and analytically integrated to give closed-form solutions:

$$\hat{\delta}^*_w = \int_{-\delta}^{\delta}\left[1 - \frac{u(y)}{U_e}\right]\mathrm{d}y = \hat{\delta}\left[1 - \frac{u_{\min}}{U_e}\right] \quad (3)$$

$$\hat{\theta}_w = \int_{-\delta}^{\delta}\frac{u(y)}{U_e}\left[1\frac{u(y)}{U_e}\right]\mathrm{d}y = \frac{\delta}{4}\left[1 + 2\frac{u_{\min}}{U_e} - 3\left[\frac{u_{\min}}{U_e}\right]^2\right] \quad (4)$$

The freestream momentum thickness θ_∞ is calculated from the local momentum thickness using the Squire–Young correction formula (see Ref. 8):

$$\theta_\infty = \theta_w[U_e/U_\infty]^{[H+5]/2} \quad (5)$$

Equation (5) corrects for the effects of the wind-tunnel blockage (described earlier) and for viscous losses along the tunnel walls. The symbol H is the wake shape parameter defined by

$$H = \delta^*_w/\theta_w \quad (6)$$

The freestream drag coefficient C_{D_0} is computed from the normalized section drag D':

$$C_{D_0} = \left[D'/\left(\rho U_\infty^2/2\right)h_{\text{base}}\right] = 2(\theta_\infty/h_{\text{base}}) \quad (7)$$

where U_∞ is the freestream velocity ahead of the model and h_{base} is the transverse height of the model base.

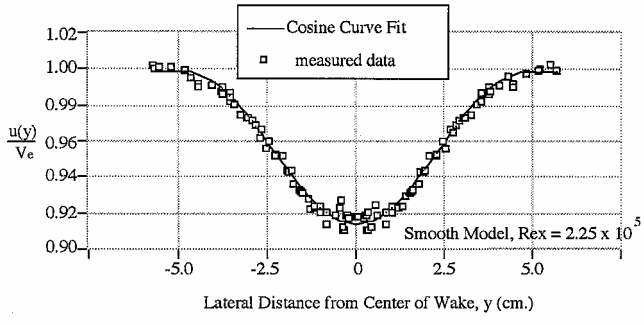

Fig. 9 Typical wind-tunnel wake velocity profile.

Boundary-Layer Velocity Profile Analysis

The forebody skin-friction coefficient is evaluated using the boundary-layer velocity profiles in a similar manner as the wake analysis presented earlier. In this case, however, Coles's law of the wake,[9] is curve fit to the local velocity profile data. The law of the wake is a general experimental correlation for turbulent boundary layers and relates the nondimensional boundary-layer velocity to the nondimensionalized boundary-layer coordinate. When expressed in velocity defect form, the law of the wake can be written as

$$\{1[u(y)/U_e]\} = \left[c_{f_x}/2\kappa^2\right]^{\frac{1}{2}}[2\Pi\cos^2[(\pi/2)(y/\delta)] - \ln[y/\delta]] \quad (8)$$

The accepted best value for κ is currently is 0.41 (Ref. 8). Π is a function of the local longitudinal pressure gradient. Das (see Refs. 8 and 10) has established an empirical correlation that relates the wake parameter to the more familiar Clauser parameter[11] β:

$$\beta = 0.42\Pi^2 + 0.76\Pi - 0.4 = \frac{2}{c_{f_x}}\frac{\delta^*}{\frac{1}{2}\rho U_e^2}\frac{\mathrm{d}P_e}{\mathrm{d}x} \quad (9)$$

where δ^* is the local displacement thickness and $\mathrm{d}P_e/\mathrm{d}x$ is at the edge of the boundary layer. Equation (9) predicts a numerical value of Π corresponding to zero pressure gradient of approximately 0.426. A value of Π value greater than 0.426 corresponds to an adverse pressure gradient, and a value of Π less than 0.426 corresponds with a favorable pressure gradient.[8] Earlier authors have placed this value at approximately 0.5 (Ref. 8) and 0.55 (Ref. 7). For this paper, the more contemporary value recommended by Das (see Refs. 8 and 10) (0.426) is used.

A nonlinear estimator similar to the procedure used earlier in the wake analysis was used extract values of c_{f_x}, Π, and δ from the boundary-layer velocity profiles. A detailed development of the nonlinear curve-fitting method used in the boundary-layer analysis is presented by Whitmore and Moes.[6] Note that the estimated value for Π is not the local pressure gradient parameter but instead should be considered as the effective wake parameter and is a composite result reflecting the averaged influence of the upstream pressure field.

Figure 10 shows an example boundary-layer curve fit compared against the wind-tunnel boundary-layer profile data. These data were obtained from the smooth model configuration tested at $Re_L = 2.25 \times 10^5$. Three individual curve fits are plotted here: a law-of-the-wake curve fit with $\Pi = 0.426$ (zero pressure gradient); a law-of-the-wake curve fit with the wake parameter adjusted to give the minimum fit error, $\Pi = 1.032$; and a one-seventh-power (turbulent) exponential curve fit. White[8] shows that a wake parameter of $\Pi = 1.032$ corresponds to a composite weak adverse pressure gradient. The model data presented in the "Results and Discussion" section support this conclusion. Clearly, the curve fit using $\Pi = 1.032$ gives a superior overall fit consistency when compared to the two other curves plotted in Fig. 10. The values for δ, c_{f_x}, and Π estimated using the boundary-layer profile data are used to calculate the local momentum and displacement thickness by integrating the law

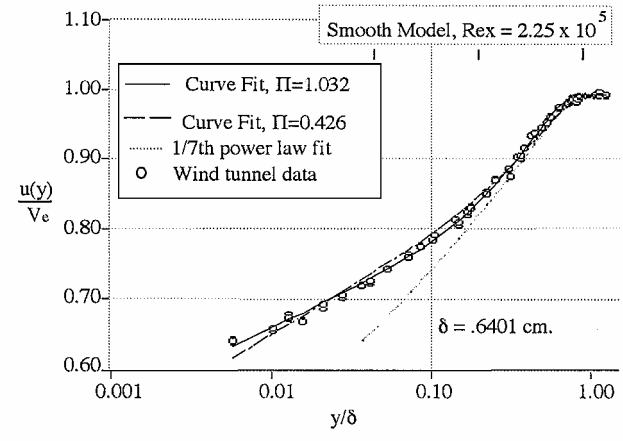

Fig. 10 Typical wind-tunnel boundary-layer velocity profile.

of the wake across the depth of the boundary layer. As derived by White,[8] the resulting expressions for the normalized displacement and momentum thickness are

$$\delta^*/\delta = \sqrt{c_{f_x}/2}[(1+\Pi)/\kappa] \tag{10}$$

$$\theta/\delta = 1/\kappa\left[c_{f_x}/2\right]^{\frac{1}{2}} \times\left\{(1+\Pi) - 1/\kappa\left[c_{f_x}/2\right]^{\frac{1}{2}}(2+3.2\Pi+1.5\Pi^2)\right\} \tag{11}$$

Once the local momentum and displacement thickness have been evaluated, then the integrated viscous forebody drag coefficient can be evaluated using the Clauser[11] form of the von Kármán momentum equation (see Ref. 8):

$$\frac{\mathrm{d}\theta}{\mathrm{d}x} = (2+H)\frac{\beta}{H}\frac{c_{f_x}}{2} + \frac{c_{f_x}}{2} \tag{12}$$

where θ is the local momentum thickness, $H = \delta^*/\theta$ is the boundary-layer shape parameter, and β is the Clauser[11] parameter. Solving Eq. (12) for the local skin-friction coefficient and integrating along the length of the model gives an approximation of the averaged forebody skin-friction coefficient C_F:

$$C_F = \frac{1}{L}\int_0^L 2\frac{\mathrm{d}\theta}{\mathrm{d}x}\frac{H}{[H+(2+H)]\hat{\beta}]}\,\mathrm{d}x \tag{13}$$

As demonstrated by Clauser,[11] for small-to-moderate pressure gradients, the boundary-layer profile shape term on the right-hand side of Eq. (13), $H/[H+(2+H)]\beta]$, is approximately constant. This feature allows easy evaluation of the integral:

$$C_F \approx 2(\theta/L)\{H/[H+(2+H)]\hat{\beta}\} \tag{14}$$

Forebody Pressure Analysis

The forebody pressure coefficient was evaluated by curve fitting the forebody pressure distribution as a function of local incidence angle Θ. For the forebody data, the seven forebody pressures were curve fit with polynomial function, and the pressure drag integral was analytically evaluated to give

$$C_{P_{\text{forebody}}} = \int_0^{\pi/2} C_p[\Theta]\cos[\Theta]\,\mathrm{d}\Theta = \int_0^{\pi/2}\left[\sum_{i=0}^{3} a_i\Theta^i\cos[\Theta]\right]\mathrm{d}\Theta = a_0 + 0.5708a_1 + 0.4674a_2 + 0.4510a_3 \tag{15}$$

Figure 11 shows a sample forebody pressure distribution plot as a function of the local incidence angle. These smooth model data were measured with the wind tunnel operating at $Re_L = 2.25\times10^5$.

Base Pressure Analysis

The base pressure coefficient was evaluated by curve fitting the base pressure distributions as a function of the lateral offset coordinate y. For the base pressure data, three base pressure ports and two aft-end ports of the flat sides of the model were curve fitted

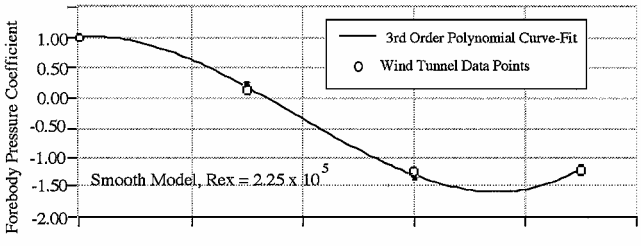

Fig. 11 Typical forebody pressure coefficient curve fit.

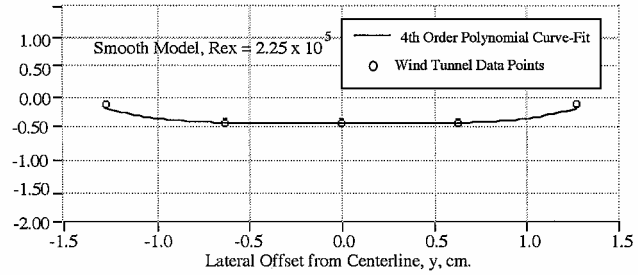

Fig. 12 Typical base pressure coefficient curve fit.

with a fourth-order polynomial. Pressure ports on the flat sides of the model were included in the curve fit to account for the taper of the base pressure near the outer edges of the model. In this curve-fitting scheme, the side ports were weighted one-half as much as the three base area ports. This weighting scheme was selected to give a base drag taper correction factor of approximately 0.925. This correction factor is suggested by Saltzman et al.[5] for full-scale flight vehicles. The base pressure drag coefficient is given by analytically evaluating the surface integral:

$$C_{D_{\text{base}}} = \int_{0.5}^{0.5} Cp[y]\,\mathrm{d}y = \int_{-0.5}^{0.5}\left[\sum_{0}^{4} b_i y^i\right]\mathrm{d}y = b_0 + 0.0833b_2 + 0.0125b_4 \tag{16}$$

Figure 12 shows a sample base pressure distribution curve fit. These data were measured on the smooth model with the wind tunnel operating at an approximate Reynolds number of $Re_L = 2.25\times10^5$.

Error Analysis

Approximations of the cumulative errors in the wake, forebody skin, forebody pressure, and base pressure drag coefficients were computed using linear analyses. The mathematical details of these analyses will not be presented in this paper, but the resulting error bars will be displayed in the "Results and Discussion" section. For the wake and boundary-layer velocity profile measurements, the first variation of the momentum thickness equation with respect to u/U_e is computed, and the resulting perturbation, $\Delta u/U_e$ is related to the mean-square curve-fit error by taking the expected value of the square of the error (perturbation) equation. For the forebody and base pressure drag coefficients, each test condition was repeated multiple times. The final estimate was the averaged value from the multiple test runs. The estimated error was computed simply as the sample-standard deviation of the values computed from multiple test points.

Results and Discussion

The wind-tunnel data clearly support the earlier computational fluid dynamics (CFD) predictions that the smooth model will lie on the suboptimal side of Hoerner's[2] curve. The suboptimal hypothesis is most clearly demonstrated by examining the base area pressure distributions. Figure 13 shows these results. The base pressure coefficients are plotted here as a function of various surface grid patterns. Figure 13a shows the pressure distributions for $Re_L = 2.25\times10^5$, and Fig. 13b shows the pressure distributions for $Re_L = 1.25\times10^5$.

Interestingly, the surface pattern with fine-mesh parallel slots and lands causes the base drag to dramatically rise (and have lower base pressure coefficients) when compared with the smooth surface model. Conversely, the surface pattern with transverse slots and lands causes the base drag to lower gradually (and have higher base pressure coefficients) when compared to the smooth surface model. Similar behavior was observed by Krishnan et al.,[12] when the authors added riblet[13] structures to the forebody of an axisymmetric wind-tunnel model with a blunt base. The authors' intents were that the riblets would lower base drag; however, the results were opposite of expectations. When the Krishnan et al. results and the data presented in Fig. 13 are interpreted considering Hoerner's[2] curve, the rising base drag is completely reasonable. The grid pattern with parallel slots and lands has the effect of acting like riblets on the model

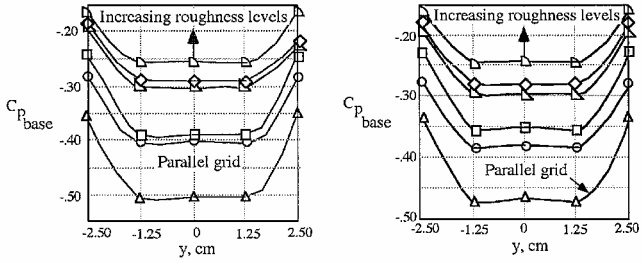

a) $Re_L = 2.25 \times 10^5$ b) $Re_L = 1.25 \times 10^5$

Fig. 13 Base pressure distributions for various grid patterns: ○, smooth model; □, transverse grid 2, $\kappa_s \sim 0.1143$ cm; ◇, transverse grid 4, $\kappa_s \sim 0.4054$ cm; △, parallel grid 1, $\kappa_s \sim 0.0163$ cm; ◺, transverse grid, 3, $\kappa_s \sim 0.2096$ cm; and ◺, transverse grid, 5, $\kappa_s \sim 0.6911$ cm.

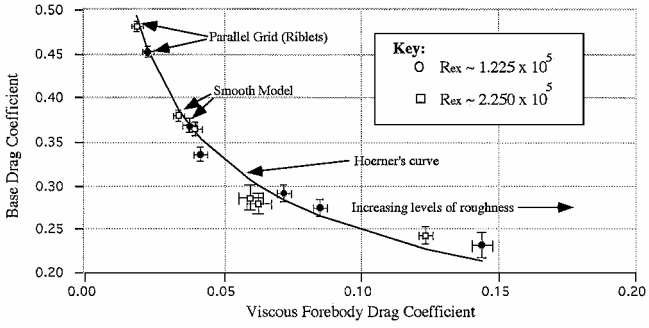

Fig. 14 Comparison of wind-tunnel base drag data vs Hoerner's[2] curve.

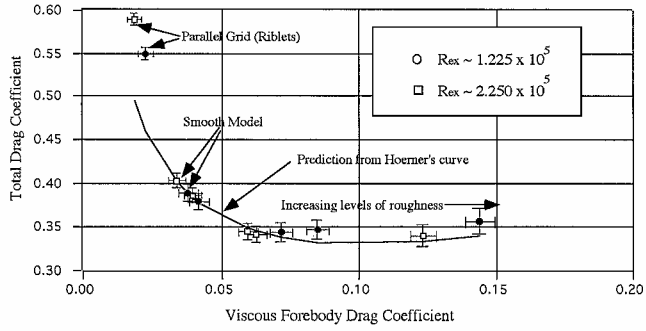

Fig. 15 Comparison of wind-tunnel wake survey data vs predicted drag bucket.

forebody. The riblet structures have the effect of lowering the forebody drag coefficient. Because the forebody skin drag coefficient is lowered, the base drag is expected to increase correspondingly. These data serve as a sort of inverse-proof of the drag-bucket theory presented in this paper. In any case, riblets should not be used in conjunction with suboptimal configurations that have highly separated base regions; their effect will cause the base drag to rise.

Figure 14 shows results from the wind-tunnel tests that further support the drag-bucket concept. The measured base drag coefficient is plotted against the viscous forebody drag coefficient calculated from the boundary-layer survey data. These data are compared to the curve fit of Hoerner's[2] two-dimensional data from Fig. 1. The open symbols represent data for 2.25×10^5, and the closed symbols represent data for 1.25×10^5. The error bars show the expected 1-σ standard deviations based on the error analyses presented earlier. The agreement with the curve fit of Hoerner's[2] data is quite reasonable.

Figure 15 shows the model total drag coefficient data (as calculated from the wake survey data) plotted against the viscous forebody drag coefficient. The error bars show the expected 1-σ standard deviations based on the error analyses discussion presented earlier. Figure 14 also shows the predicted drag curve defined using Hoerner's[2] two-dimensional curve from Fig. 1, the viscous forebody drag measurement, and the model forebody drag coefficient

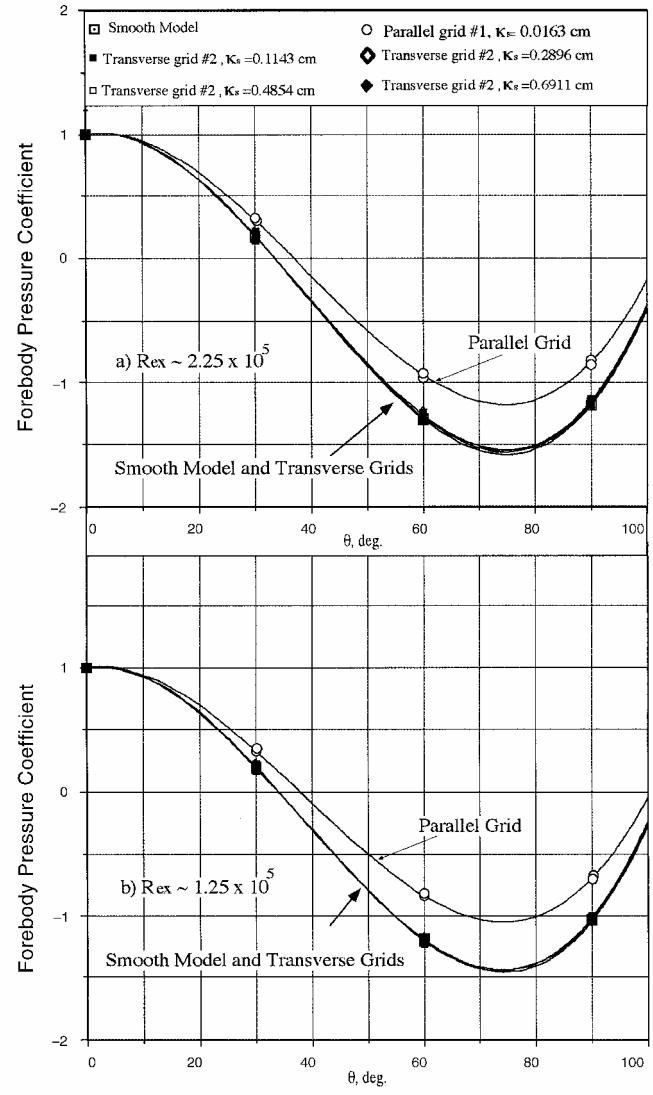

Fig. 16 Forebody pressure distributions for various grid patterns.

(approximately −0.018) predicted by CFD solutions.[6] Except for the parallel grid (riblet) data, the agreement with the predicted drag curve is excellent.

The disagreement for the parallel grid test points is caused by a sharp rise in the forebody pressure coefficients. Figure 16 shows these data. The forebody pressure distributions for all of the grids are plotted here as a function of the local incidence angle. Figure 16a shows the higher-Reynolds-number data and Fig. 16b shows lower-Reynolds-number data. The transverse grid patterns do not significantly alter the forebody pressure distribution; however, the forebody pressure data are considerably higher for the parallel grid pattern. The parallel grid data are clearly an anomaly. The reasons for this pressure anomaly are not clear at this point, but the parallel grid possibly caused relaminarization of the flow and induced a localized separation. This anomaly requires further investigation.

Most important, the data shown in Fig. 16 demonstrate the existence of a drag minimum with regard to the viscous forebody drag coefficient. The elusive drag bucket is clearly defined, and the primary hypothesis of this paper is conclusively proven. The drag reduction from the smooth model configuration to the optimum point is approximately 15%. Also, comparison of Fig. 15 with Fig. 16 shows that the base drag coefficient corresponding to the total drag coefficient minimum lies somewhere between 0.225 and 0.275. This value is a bit lower than the 0.25–0.30 range predicted by analysis of Hoerner's[2] original data.

Conclusions

This paper presents results of wind-tunnel tests that demonstrate a novel drag reduction technique for blunt-based vehicles. For blunt-based bodies, a direct correlation exists between base and viscous forebody drag. As the forebody drag coefficient increases, the base drag of the projectile generally tends to decrease. This base drag reduction results from boundary-layer effects at the vehicle base. When the added increment in forebody skin drag is optimized with respect to the base drag reduction, then reducing the overall drag of the configuration is possible. In these tests, a two-dimensional cylinder with a blunt after-body was tested.

The wind-tunnel results conclusively demonstrate existence of a forebody drag optimum. Also, the wind-tunnel data demonstrate that the base drag coefficient corresponding to the total drag minimum lies somewhere between 0.225 and 0.275. This optimality point is slightly lower than the 0.25–0.30 range predicted by analysis of Hoerner's[2] original data. The use of parallel grid lines that emulate the effects of riblet structures on bodies with highly separated base regions will likely cause the total drag of the configuration to rise. Most important, the data show a peak drag reduction at approximately 15%.

Because this drag reduction technology is still immature, the practical limits of applicability are unknown at this point. However, a wide spectrum of potential users exists, including the aerospace, automotive, ground transport, and shipping industries. This drag reduction technique offers the potential for decreased operating costs resulting from decreased overall fuel consumption.

References

[1]Wong, T. J., Hermach, C. A., Reller, J. O., Jr., and Tinling, B. E., "Preliminary Studies of Manned Satellites—Wingless Configurations: Lifting Body," *NACA Conference on High-Speed Aerodynamics: A Compilation of the Papers Presented*, NASA TM-X-67369, 1958, pp. 35–44.

[2]Hoerner, S. F., *Fluid-Dynamic Drag: Practical Information on Aerodynamic Drag and Hydrodynamic Resistance*, Self-published work, Library of Congress Card Number 64-19666, Washington, DC, 1965.

[3]Tanner, M., "Theories for Base Pressure in Incompressible Steady Base Flow," *Progress in Aerospace Sciences*, Vol. 34, 1998, pp. 423–480.

[4]Rathakrishnan, E., "Effect of Splitter Plate on Bluff Body Drag," *AIAA Journal*, Vol. 37, No. 9, 1999, pp. 1125, 1126.

[5]Saltzman, E. J., Wang, K. C., and Iliff, K. W., "Flight-Determined Subsonic Lift and Drag Characteristics of Seven Lifting-Body and Wing-Body Reentry Vehicle Configurations with Truncated Bases," AIAA Paper 99-0383, Jan. 1999.

[6]Whitmore, S. A., and Moes, T. R., "Base Drag Reduction Experiment on the X-33 Linear Aerospike SR-71 Flight Experiment (LASRE)," AIAA Paper 99-0277, Jan. 1999.

[7]Mills, A. F., *Heat and Mass Transfer*, 2nd ed., Irwin, Burr Ridge, IL, 1995, pp. 267–325.

[8]White, F. M., *Viscous Fluid Flow*, 2nd ed., McGraw–Hill, New York, 1991, pp. 325–498.

[9]Coles, D., "The Law of the Wake in the Turbulent Boundary Layer," *Journal of Fluid Mechanics*, Vol. 1, 1955, pp. 191–226.

[10]Whitmore, S. A., Hurtado, M., Rivera, J., and Naughton, J. W., "Real-Time Method for Estimating Viscous Forebody Drag Coefficients," AIAA Paper 2000-0781, Jan. 2000.

[11]Clauser, F. H., "Turbulent Boundary Layers in Adverse Pressure Gradients," *Journal of the Aeronautical Sciences*, Vol. 21, No. 2, 1954, pp. 91–108.

[12]Krishnan, V., Viswanath, P. R., and Rudrakumar, S., "Effects of Riblets on Axisymmetric Base Pressure," *Journal of Spacecraft and Rockets*, Vol. 34, No. 2, 1997, pp. 256–258.

[13]Walsh, M. J., "Riblets as a Viscous Drag Reduction Technique," *AIAA Journal*, Vol. 21, No. 4, 1983, pp. 485, 486.

M. S. Miller
Associate Editor